Title
Quantum disordered ground state in the triangular-lattice magnet $NaRuO_2$

Journal
Nature Physics, 19(7)

ISSN
1745-2473 1745-2481

Authors
Ortiz, Brenden R
Sarte, Paul M
Avidor, Alon Hendler
et al.

Publication Date
2023-04-24

DOI
10.1038/s41567-023-02039-x

Peer reviewed

Quantum Disordered Ground State in the Heisenberg-Kitaev Candidate $NaRuO_2$

Brenden R. Ortiz[1#], Paul M. Sarte[1#], Alon Hendler Avidor[1], Aurland Hay[1], Eric Kenney[2], Alexander I. Kolisneikov[3], Daniel M. Pajerowski[3], Adam A. Aczel[3], Keith M. Taddei[3], Craig M. Brown[4,5], Chennan Wang[6], Michael J. Graf[2], Ram Seshadri[1], Leon Balents[7], Stephen D. Wilson[1*]

[1] Materials Department, University of California, Santa Barbara, California 93106, USA
[2] Department of Physics, Boston College, Chestnut Hill, Massachusetts 02467, USA
[3] Neutron Scattering Division, Oak Ridge National Laboratory, Oak Ridge, TN 37831, USA
[4] NIST Center for Neutron Research, National Institute of Standards and Technology, Gaithersburg, Maryland 20899, USA
[5] Chemical and Biomolecular Engineering, University of Delaware, Newark, Delaware 19716, USA
[6] Laboratory for Muon Spin Spectroscopy, Paul Scherrer Institute, 5232 Villigen, Switzerland
[7] Kavli Institute for Theoretical Physics, University of California, Santa Barbara, Santa Barbara, California 93106, USA.
[*] stephendwilson@ucsb.edu
[#] these authors contributed equally to this work

The realization of spin liquid states born from the near-critical regime of the triangular lattice Hubbard model in inorganic materials remains a long-standing challenge, where weak spin-orbit coupling and other small perturbations often induce conventional spin freezing or order. Strong enough spin-orbit coupling, however, can renormalize the electronic wave function and induced anisotropic exchange interactions that promote magnetic frustration. Through the cooperative interplay of spin-orbit coupling and correlation effects, here we show that the triangular lattice magnet $NaRuO_2$ hosts an inherently fluctuating magnetic ground state with thermodynamic properties suggestive of a crossover between dynamic ground states. Despite the presence of a charge gap, we find that low-temperature spin excitations generate a metal-like term in the specific heat and continuum excitations in neutron scattering, reminiscent of spin liquid states found in triangular lattice organic magnets. Further cooling reveals that these fluctuations crossover into a state whose dynamic spin autocorrelation function reflects persistent fluctuations within a highly disordered spin state. These findings instantiate $NaRuO_2$ as a unique, Heisenberg-Kitaev cousin to organic, Heisenberg spin liquid compounds with a low-temperature crossover in quantum disorder driven via the interplay between geometric frustration, extended hopping, and relativistic spin-orbit coupling.

The interplay between electron-electron correlation effects and geometrical frustration can lead to a rich hierarchy of electronic states. The Hubbard model at half-filling shows that, as the on-site Coulomb interaction (U) is reduced relative to the electron hopping energy (t), the ground state transitions from an antiferromagnetic insulating state into a nonmagnetic metal. If the underlying lattice is triangular, then an intermediate nonmagnetic insulating state is predicted prior to the onset of the metallic state[1,2,3]. The predicted properties of this intermediate phase vary depending on the theoretical approach, however it is generally envisioned as an inherently quantum disordered magnetic state or a quantum spin liquid phase generically realized at the boundary of the Mott insulating regime.

Proposed physical manifestations of this type of spin liquid state are rare, with well-studied candidates identified in anisotropic triangular magnets built from organic molecular complexes[4,5,6,7]. In inorganic compounds, however, triangular lattice systems identified thus far are located either deep in the insulating regime,[8] deep in the metallic state,[9] or better described in the strong coupling limit via a pure

Heisenberg model.[10] One promising means of more fully exploring this materials space is to consider compounds with extended *d*-electron orbitals, where the cooperative interplay between moderate on-site Coulomb repulsion (U) and spin-orbit coupling (λ) driven bandwidth narrowing can generate marginally stable J_{eff}=1/2 Mott insulating states with $U/t\approx1$.[11] Such states are known to form in *5d*-transition metal iridates, where controlling the bandwidth can drive a metal-insulator transition,[12] and similarly, weak J_{eff}=1/2 Mott states may also be realized in *4d*-transition metal compounds.[13]

Specifically, Ru^{3+} ($4d^5$) ions in a nearly cubic crystal field are capable of assuming a low-spin state with both λ and U appreciable enough to stabilize a half-filled J_{eff}=1/2 orbital.[14,15] An ideal triangular lattice consisting of octahedrally coordinated Ru^{3+} moments is also known to form in delafossite variants such as $NaRuO_2$,[16] which suggests an opportune setting for searching for an intermediate quantum disordered state at the boundary of the J_{eff}=1/2 Mott state's stability. Remarkably little is known regarding the ground state of this compound and, more generally, whether it can provide a suitable experimental window into the electronic properties of a near-critical triangular lattice Hubbard model in the presence of strong λ.

Here we establish that $NaRuO_2$ hosts electrons in a unique interaction space as an ideal triangular lattice possessing a weak spin-orbit assisted Mott insulating ground state—one consistent with the expectation of a near-critical J_{eff}=1/2 Mott state driven by cooperative λ and U. Through studies of polycrystalline samples, our data demonstrate that despite the presence of a charge gap, the high-temperature magnetism of $NaRuO_2$ shows an elevated Pauli-like susceptibility, and at low temperatures, where the charge gap is well established, heat capacity data show a substantial linear term akin to the Sommerfeld coefficients expected in metals. The magnetic excitations comprising this linear term generate a diffuse continuum of spin excitations, a portion of which are slowed down below a field-coupled crossover into a state with persistent fluctuations and a heat capacity quadratic in temperature. Our data demonstrate that J_{eff}=1/2 electrons built from extended *d*-orbitals on a triangular lattice stabilize quantum disordered magnetic phase behavior, consistent with expectations of Hubbard models near the metal-insulator phase boundary[17] as well as models of Kitaev antiferromagnets.[18,19]

Figure 1 (a) shows the detailed crystal structure of $NaRuO_2$. Edge-sharing RuO_6 octahedra form a triangular lattice of Ru^{3+} ions separated by planes of Na ions. An ideal equilateral triangular lattice results and a slight (< 5°) trigonal distortion exists in the oxygen octahedra surrounding the Ru ions. Neutron diffraction data presented in Fig. 1 (b) show fully occupied Na and O sites and no site mixing with the resolution of the measurement. The predominant defect mode within $NaRuO_2$ is Na_{Ru} antisite defect formation, which can be avoided by synthesizing samples in a slightly Ru-rich environment.[20] Furthermore, neutron powder diffraction data collected at temperatures as low as 50 mK show no signs of structural symmetry breaking or static spin correlations forming between Ru moments. This is remarkable given the large covalency and enhanced exchange expected between the extended Ru moments, which are only 3.06 Å apart.

Ab initio electronic structure calculations shown in Fig. 1 (c) reveal that the band structure of $NaRuO_2$ is highly sensitive to the structural parameters. Using the experimentally-derived structure in this paper, a charge gap forms via inclusion of both λ and U using the local density approximation (LDA). Choosing U=1 eV, consistent with prior LDA + λ + U models of Ru^{3+} systems such as $RuCl_3$,[21] opens a gap when incorporated with λ. However, the model and the prediction of the presence or absence of a gap is highly sensitive to the local distortions of oxygen octahedra around the Ru sites—consistent with the notion of a marginally insulating state where extended hopping effects can play an important role. The resistivity data presented in Fig. 2 (a) verify that $NaRuO_2$ indeed possesses an insulating ground state whose electrical transport is best modeled via a two-dimensional variable range hopping; however we note that discrimination between two-dimensional and three-dimensional forms is difficult in polycrystalline samples. If the data above 200 K are parameterized by forcing an Arrhenius fit, the apparent gap value is $E_g \approx 0.22$ eV.

Contrasting the electrical transport data, the temperature-dependent magnetic susceptibility data presented in Fig. 2 (b) instead show a nearly itinerant magnetic response. The weak increase in the susceptibility upon cooling does not fit to a conventional Curie-Weiss form, and instead, the low-temperature susceptibility is best fit to a large Pauli-like term (χ_0) with a weak concentration of free impurity moments (1.8±0.2% of S=1/2 moments). Notably, the χ_0 term is unusually large for an insulator, $\chi_0=9.6\pm0.2\times10^{-4}$ emu Oe^{-1} mol^{-1}, a value exceeding that of Pd metal with $\chi_0=7.3\times10^{-4}$ emu Oe^{-1} mol^{-1} at 4 K).[22] As a consistency check, the large χ_0 fit via the temperature dependent magnetization matches the linear term found in the isothermal magnetization ($\chi_0=1.25\pm0.1\times10^{-3}$ emu Oe^{-1} mol^{-1}), which can be parameterized by a dominant Pauli-like linear term and a small fraction of S=1/2 moments (1.4±0.2%) shown in Fig. 2 (c). At lower temperatures, a weak cusp appears in the susceptibility data below 1.5 K, as shown in the inset of Fig. 2 (b). There is a weak frequency dependence to the onset of this cusp as shown in Supplemental Figure 2, which deviates from the expectations of a canonical spin glass, but nevertheless suggests a weak freezing in the local moment contribution to the overall susceptibility. The nature of this slowdown in the dynamics will be discussed later in this paper.

Exploring this further, heat capacity data were collected down to 80 mK and are plotted in Fig. 2 (d). As the system is cooled far below the Debye temperature, $C_p(T)$ takes on the form $C_p(T)=\gamma T+\beta T^3$ where β parameterizes the contribution from phonons and γ is an anomalous linear term typically observed in metals. In free electron gases, γ represents the Sommerfeld coefficient—a term proportional to the electronic density of states occupied at the Fermi level; however in magnetically frustrated insulators the presence of a γ term suggests a fractionalization of electrons and the presence of a spinon Fermi surface. The γ term in $NaRuO_2$ is substantial (14.07±0.12 mJ $mole^{-1}$ K^{-2}) and is distinct from the small γ's found in disordered insulators such as TiO_2 (0.1 mJ $mole^{-1}$ K^{-2}).[23,24] Instead, it is comparable in magnitude to those found in organic triangular lattice spin liquid candidates.[25,26,27] One notable distinction is that the presence of strong spin-orbit coupling amplifies χ_0 and the resulting Wilson ratio $R_W = \frac{\pi^2 k_B^2 \chi_0}{3\mu_B^2\gamma}$ = 8 for $NaRuO_2$ versus $R_W \approx 1$ for organic compounds.

Cooling below 2 K reveals the onset of a weak freezing transition in $C_p(T)$ matching the cusp in the low-T susceptibility. Only a small amount of entropy is associated with this T_F = 2 K crossover (1.2±0.2% of $R\ln(2)$) further correlating it with a freezing of a small fraction of local moments. However, T_F also marks the onset of a modified power law behavior $C_p(T)=AT^{\alpha}$ that depends on the magnetic field. Applying a magnetic field shifts this T_F crossover upward in temperature, and, as the shoulder of this freezing feature shifts to higher temperatures, the low temperature $C_p(T)$ converges to a quadratic behavior (α = 2). Notably, the application of a magnetic field also enhances the apparent γ term above T_F, and it increases by 21% under μ_0H = 14 T. We note that the magnetic entropy estimate shown in the inset of Fig. 2 (d) becomes increasingly unreliable at higher temperatures due to an imperfect subtraction of the lattice contribution in the regime where magnetic fluctuations become substantially weaker compared to the phonon contributions. This potentially generates the weakly nonsaturating response.

To investigate the nature of the magnetic excitations associated with these low energy fluctuations, inelastic neutron scattering measurements were performed. As an initial survey, temperature subtracted data (1.8 K -300 K) are plotted in Fig. 3 (a), where magnetic spectral weight at low momentum transfers appears centered near 25 meV. Energy cuts (integrated over small momentum transfers *Q*) of unsubtracted data are plotted for both the 1.8 K and 300 K datasets in Fig. 3 (b) and show a peak in scattering at 1.8 K that is broadened, diminished, and shifted downward in energy upon warming to 300 K. A similar subtraction of the data for a lower incident energy is also shown in Fig. 3 (c). The momentum distribution of the resulting gapless, low-energy continuum is centered near 1.2 Å^{-1} as shown in Fig. 3 (d).

The broad continuum is further investigated at lower incident energies and temperatures (250 mK) in Fig. 3 (e). Spin fluctuations are gapless down to 0.1 meV with spectral weight centered at finite momentum near **Q**=1.2 Å^{-1} as well as along low angles suggestive of fluctuations centered at **Q**=0. Upon warming to 12 K (across the 1.5 K cusp in $\chi'(T)$ and $C_p(T)$), these low energy spin fluctuations are nearly temperature independent. Energy cuts through both finite momentum and low-angle spectral weights are shown in Figs. 3 (f) and (g) respectively. In both cases, excitations where the system gains energy (*E*>0) are nearly temperature independent while excitations where the system loses energy (*E*<0) populate up with increasing temperature and follow detailed balance. This behavior in $S(Q,E)$ suggests quantum critical fluctuations in $\chi''(Q,E) = S(Q,E)(1-e^{-E/k_BT})$ that potentially scale as a function of *E/T*. The low energy data was tested for quantum critical scaling where $\chi''(Q,E)T^{\alpha} \propto f\left(\frac{E}{T}\right)$ by analyzing collapse to a test function $f\left(\frac{E}{T}\right) = \frac{\left(\frac{E}{T}\right)^{\alpha}}{\left(\frac{E}{T}\right)^{2\alpha}+\beta}$. Scaling collapse was optimized for $\alpha = 0.83 \pm 0.05$ and, though this test function is phenomenological, it reproduces the asymptotic *E/T*>>1 form $f\left(\frac{E}{T}\right) \approx \left(\frac{E}{T}\right)^{-\alpha}$ expected in a number of quantum critical scaling relations.[28,29] The collapse of the data linked by this asymptotic form is consistent with robust quantum fluctuations present in the magnetic ground state of $NaRuO_2$.

To probe the spin dynamics at even lower frequencies, the muon spin relaxation technique was used for the determination of different static local fields and the presence of magnetic fluctuations. The temperature dependent muon polarization and their fit are presented in Fig. 4(a). At 12 K, the muon spin depolarization is best described via a Gaussian Kubo-Toyabe form dominated by the contribution of nuclear moments in the sample. Upon cooling below 12 K, the magnetic fluctuations from the antiferromagnetically coupled electronic spins slow down into the muon time window and the time-dependent polarization is described by a generalized depolarization function $P(t) = (f)GbG(\Delta;R;t)e^{(-\lambda_{GbG}t)^{\beta}} + (1-f)e^{-\lambda_p t}$. This is a response comprised of an uncorrelated fraction $(1-f)$ of paramagnetic moments whose fluctuations drive simple exponential relaxation at λ_p that, upon cooling, converts into a highly disordered response captured by a Gaussian-Broadened-Gaussian (GbG) function supplemented by spin fluctuations in the form of a stretched exponential with relaxation rate λ_{GbG}. The GbG function[30] represents a normal distribution of Gaussian field distributions about a central value Δ_0 with width *w* captured by the parameter $R = w/\Delta_0$. As shown in Fig. 4(b), Δ_0 increases progressively with decreasing the temperature below 3 K, and *R* becomes finite at approximately 2.5 K, with the value trending toward 1 at base temperature. The absence of clear oscillatory signals suggests that the low-temperature state contains intermediate-diluted and disordered static magnetic moments. Meanwhile, this nominally static distribution of fields is modified by a slow fluctuation rate (λ_{GbG}) as presented in Fig. 4(c), similar to other highly frustrated materials with persistent spin fluctuations in their ground states[31]. To discriminate the presence of persistent fluctuations in this disordered ground state versus depolarization via static disorder, a longitudinal field (LF) experiment was performed. Such a field rapidly decouples muons from slow depolarization due to purely static field distributions, whereas depolarization persists in systems that are inherently dynamic[32]. The data in Fig. 4 (d) indicate the persistence of fluctuations under modest applied fields, for example, contrasting the rapid decoupling seen in static field distributions in frustrated, yet statically frozen systems such as $Na_4Ir_3O_8$.[33,34]

To further distinguish the partial freezing and persistent dynamics in $NaRuO_2$ from conventional spin glass behavior, we demonstrate the magnetic-field time scaling relations of the LF time-spectra using the form $P(H, t)=P(t/H^{\gamma})$.[35] The polarization maps to the spin autocorrelation function, and, above the freezing temperature, the depolarization should scale as a function of t/H^{γ} with the scaling exponent γ reflective of the manner through which spin correlations decay in time.[36] With the exception of the short-time limit $\mu_0H = 0.02$ T data, the data scale well to this form with the analysis shown in Figs. 4 (e) and (f) and the R^2 of scaled data versus a test polynomial is shown in Fig. 4(f)'s inset. This scaling analysis yields an exponent of $\gamma \approx 1.75$, which precludes conventional spin-glass power law correlations ($\gamma \leq 1$) and, instead, is consistent with the expectation of decay via a stretched exponential function—identical to the type used to model the zero-field data.

The above experimental picture suggests that $NaRuO_2$ occupies a unique phase space where a spin-orbit assisted Mott state gives rise to a native quantum disordered ground state. Charge fluctuations as well as anisotropic Kitaev interactions potentially play an important role in this disordered state. Ru^{3+} ions sit in a nearly cubic crystal field quantified by a quadratic elongation parameter[37] $\lambda_{quad}=1.0074$, similar to that observed in Na_2IrO_3.[38] This should promote the formation of a $J_{eff}=1/2$ wavefunction from the t_{2g} orbital manifold. An array of such wavefunctions on a honeycomb lattice composed of edge-sharing octahedra generates strong Kitaev exchange and is predicted to stabilize a quantum spin liquid ground state, but experimental realizations are lacking. Although materials such as Na_2IrO_3[39] and $RuCl_3$[40] are known to stabilize strong ferromagnetic Kitaev coupling strengths, due to dominant Heisenberg interactions they nevertheless possess magnetically ordered ground states.[41,42] Similar predictions of dominant Kitaev exchange and quantum spin liquid phases have also been put forward for $J_{eff}=1/2$ electrons decorating a triangular lattice.[19] However, unlike other Kitaev candidate materials, the thermodynamic phenomenology of $NaRuO_2$ resembles that of highly frustrated organic spin liquids and additional interactions such as charge fluctuations may play a role. We hypothesize this is due to the weak nature of the insulating state and added importance of longer-range exchange interactions. These ingredients are believed to stabilize intrinsically quantum disordered ground states[43,44] as we propose is realized here.

Inorganic compounds with simple structures and large magnetic exchange energy scales rarely realize quantum disordered or spin liquid-type ground states due to low-energy interactions, such as Dzyaloshinskii-Moriya interactions or weak lattice distortions that lift magnetic frustration. Even rarer is a quantum spin liquid candidate that manifests a transition/crossover between quantum disordered phases manifest in the breakdown of the γ term in $NaRuO_2$. The unique interplay between the marginally insulating Mott state and anisotropic exchange fostered by cooperative spin-orbit coupling and on-site Coulomb interactions suggests that $NaRuO_2$ occupies a unique energy landscape—one where Kitaev coupling in the Hubbard model fosters nearby quantum disordered states. The result is a material that provides an appealing opportunity for pushing the manifestation of exotic phenomena such nonabelian quasiparticle excitations associated with a native spin liquid state up to higher temperatures for future quantum information applications.

Methods:

Sample preparation: Polycrystalline $NaRuO_2$ was synthesized using mechanochemical methods. Sodium peroxide (Na_2O_2) beads (Sigma, 97%), ruthenium dioxide (RuO_2) powder (Alfa, 99.95%), and Na metal (Alfa 99.8%) are combined in a pre-seasoned tungsten carbide ball-mill vial under argon. The synthesis generally needs excess Na and O during the reaction; though we note that $NaRuO_2$ exhibits an unusually large degree of off-stoichiometry in the Na-rich regime. To optimize purity and Na-stoichiometry, we have designed the synthesis to minimize Na_{Ru} antisite defects by forcing $NaRuO_2$ to crystallize in equilibrium with Ru and $NaRu_2O_4$, which corresponds to the Ru-rich edge of the phase diagram. Thus, the stoichiometry has been tuned empirically to $Na_{1.07}(Na_2O_2)_{0.35}(RuO_2)_{1.35}$. A more detailed analysis of the phase diagram and the resulting Na_{Ru} off-stoichiometry can be found in Ortiz et al.[20].

The resulting mixture is milled for 60 minutes in a Spex 8000D Mixer/Mill using four 7.9mm tungsten carbide balls. The reaction generates a substantial amount of heat, and precursor powders produced through milling are effectively amorphous. Resulting precursor powder is lightly ground in an agate mortar, sieved through a 100 micron sieve, and loaded into 2mL CoorsTek alumina crucibles. Small quantities of precursor are also pressed into discs with a Carver press and subsequently buried in the precursor powder. The crucibles are sealed under approximately 1 bar of argon in fused silica ampoules and immediately placed within a preheated furnace at 900°C. Samples are annealed for 30min and are then immediately air-quenched before extracting powders within an argon glovebox with water and O_2 levels <0.5ppm. In the anneal, both the pellet and powder transform into the desired phase, while the pellet simultaneously densifies (sinters). This ensures that sample preparation is consistent throughout all measurement probes. Resulting powders are largely phase pure with trace amounts of Ru metal (<1%) and Na_2CO_3 (<3%) due to an impurity in the starting Na_2O_2 reagent. Powders are black and are highly moisture sensitive.

$NaRhO_2$ powder was prepared and sintered for a phonon reference in heat capacity measurements for estimating the magnetic entropy. It was prepared following the methods reported in Verger et al. [45] and the phase purity was confirmed via x-ray diffraction (Supplementary Figure 5).

X-ray Synchrotron diffraction: High-resolution synchrotron powder diffraction data were collected using beamline 11-BM at the Advanced Photon Source (APS), Argonne National Laboratory using an average wavelength of 0.457925 Å. Both 300 K and 5K measurements were performed to check for any crystallographic phase transformations, and for better analysis of thermal parameters and occupancies at base temperatures. Discrete detectors covering an angular range from -6 to 16° in 2θ are scanned over a 34° range, with data points collected every 0.001°, and scan speed of 0.01°/s. Due to the air sensitivity of the materials, small quantities of $NaRuO_2$ were diluted with amorphous SiO_2 in a glovebox and sealed under argon in flame-tipped amorphous SiO_2 capillaries. These capillaries were nested within kapton sleeves and held in place with a small amount of modeling clay. The resulting data, and pattern refinement are shown in Supplemental Figure 1 and the structural parameters summarized in Supplemental Table 1. Diagnostic laboratory powder diffraction utilized a Panalytical Empyrean diffractometer (Cu Kα, 1.54 Å) in the Bragg-Brentano geometry.

Neutron diffraction: Neutron powder diffraction measurements were performed on the fixed incident energy triple-axis spectrometer HB-1A (λ=2.37 Å) of the High Flux Isotope Reactor (HFIR) at ORNL. 6 grams of phase pure polycrystalline $NaRuO_2$ was loaded in a cylindrical Cu can which was then placed in a dilution insert of an orange cryostat, providing a base temperature of 50 mK. The collimation configuration of 40'-40'-40'-80' selected yielded an energy resolution (FWHM) at the elastic line of ~ 1 meV. The combination of the double-bounce monochromator system and the placement of the pyrolytic graphite (PG) crystal analyzer for energy discrimination before the single He-3 detector provided an excellent signal-to-noise ratio. Additional contamination from higher-order wavelength contamination was minimized with the use of two PG filters.

High resolution neutron powder diffraction experiments were performed on the high-resolution neutron powder diffractometer BT-1 of the NIST Center for Neutron Research (NCNR) at the National Institute of Standards and Technology (NIST). A Ge(311) monochromator provided a λ=2.0772 Å with maximum neutron flux, allowing for full diffraction patterns to be collected in 12 hours. 4.5 grams of phase pure polycrystalline $NaRuO_2$ was loaded into a vanadium can under a He atmosphere and placed into a top loading flow-type orange cryostat, providing a base temperature of 1.6 K. Rietveld refinements of the neutron diffractograms were performed with TOPAS Academic V6 with the results shown in Supplemental Table 1.

Inelastic neutron scattering: High-energy inelastic neutron scattering experiments were performed on the direct geometry time-of-flight chopper spectrometer SEQUOIA of the Spallation Neutron Source (SNS) at Oak Ridge National Laboratory.[46] 8 grams of phase pure polycrystalline NaRuO2 was loaded in a cylindrical Al can which was placed in a top loading helium cryostat, providing a base temperature of 1.8 K. Powder-averaged (Q,E) spectra were collected with incident energies of E_i=80 meV and 42 meV, operating in high flux mode, providing an elastic resolution of ≈7.8% and ≈2.3% E_i, respectively. Background contributions to the inelastic spectra were approximated by measurement of an empty aluminum can, which was measured in identical experimental conditions for approximately one third of the counting time allocated for the sample. Scattering maps shown in Figures 3 (a) and (c) are temperature subtracted data corrected for the Bose population factor obtained via $\left(S(Q,E)_{sample,1.8K} - S(Q,E)_{can,1.8K}\right) - A(E)\left(S(Q,E)_{sample,300K} - S(Q,E)_{can,300K}\right)$, where $A(E)$ is the ratio of the Bose-factors $A(E) = \left(1 - e^{-E/k_B T}\right)_{T=1.8K} \Big/ \left(1 - e^{-E/k_B T}\right)_{T=300K}$ for each E value. Cuts in Figure 3 (b) are cuts through $\left(S(Q,E)_{sample} - S(Q,E)_{can}\right)$ data at T=1.8 K and T=300 K.

Low-energy inelastic neutron scattering experiments were performed on the direct geometry time-of-flight chopper spectrometer CNCS of the SNS. Approximately 9 grams of $NaRuO_2$ was loaded under insert atmosphere in a cylindrical Cu can which was placed onto a HelioxVT A-100mm ^{3}He insert in a top loading 100 mm orange cryostat, providing a base temperature of 250 mK. Powder-averaged (Q,E) spectra were collected with incident energies of 3.32 meV and 1.55 meV, operating in high flux (HF) mode, providing an elastic resolution of 0.1 and 0.03 meV, respectively.[47] Background contributions to the inelastic spectra were approximated by an empty Cu can, which was measured in identical experimental conditions with equal counting times that were allocated for the sample and removed from the data. Normalization with a vanadium standard was performed to account for variations of the detector response and the solid angle coverage. Additional background subtracted maps of S(Q,E) used for the scaling analysis data are presented in Supplemental Figures 6 and 7.

Magnetic Susceptibility (MPMS, PPMS, and ACDR): The temperature dependence of the zero-field-cooled (ZFC) and field-cooled (FC) DC magnetization of 17.6 mg of phase pure $NaRuO_2$ powder placed in a brass holder was measured on a 7 T Quantum Design Magnetic Property Measurement System (MPMS3) SQUID magnetometer. Data was collected continuously in sweep mode with a ramp rate of 2 K/min in the presence of an external DC field of 1000 Oe (1 Oe = (1000/4π) A/m). The fit Pauli-like χ_0 was corrected for core diamagnetism (-53.8E-6 emu/mol/Oe).[48]

Isothermal magnetization measurements of the same 17.6 mg $NaRuO_2$ sample at 1.8 K and 300 K were performed on a Quantum Design 14 T Dynacool Physical Property Measurement System (PPMS) employing the vibrating sample magnetometer (VSM) option. ZFC data was collected continuously in sweep mode with a ramp rate of 100 Oe/sec .

The temperature dependence of the ac magnetization of 10.1 mg of phase pure $NaRuO_2$ powder was measured on a Quantum Design 14 T Dynacool PPMS employing the ac susceptibility option for the dilution refrigerator (ACDR). A portion of a sintered pellet with approximate dimensions of 1 mm x 1 mm x 0.5 mm was adhered to a quartz sample mounting post with a thin layer of GE-varnish. All ac measurements were collected in stable mode under ZFC conditions in an external DC magnetic field of 1 T and with a ramp rate of 0.08 K/min.

Heat Capacity: The temperature and field dependence of the specific heat capacity of a 5.62 mg fragment of a phase pure $NaRuO_2$ sintered pellet and 6.21 mg of its non-magnetic analog $NaRhO_2$ were measured on a Quantum Design 14 T Dynacool PPMS employing the heat capacity (HC) option. Apiezon N grease was used to optimize thermal coupling between the sample and calorimeter stage. All measurements were performed upon heating, while all measurements in field were done in ZFC conditions. The phonon contribution was removed for estimating the magnetic entropy only, and this was achieved via subtraction of a $NaRhO_2$ standard sample.

SPS: $NaRuO_2$ pellets (10 mm diameter x 2 mm thick) were prepared from phase pure $NaRuO_2$ powder using field-assisted sintering (FCT Systeme GmbH, Frankenblick, Germany). The pellets were pressed at 850 °C and 90 MPa for 60 min in an Ar-filled chamber with a pressure of 30 hPa, using a heating rate of 150 °C/min and a cooling rate of 40 °C/min. All pellets were subsequently ground to a 2000-grit finish before resistivity measurements. Note that SPS samples were primarily used to test the influence of grain-boundary effects by producing samples with a variety of experimental densities, as detailed in Supplemental Figure 4.

Resistivity: $NaRuO_2$ sintered pellets were sectioned into rectangular bars with dimensions approximately 1 mm x 2 mm x 0.5 mm. Electrical contacts were made in a standard four-point geometry with contacts being made with a combination of gold wire and silver paint. The paint used was DuPont cp4929N-100, and the gold wire used for leads is Alfa Aesar 0.05mm Premion 99.995%. Thermal contact and electrical isolation was ensured using layers of GE varnish and cigarette paper. The temperature dependence of the electrical resistivity was measured with the Electrical Transport Option (ETO) on a 9 T Quantum Design Dynacool PPMS using a drive current of 10 μA and drive frequency of 100 Hz. Data was collected continuously in sweep mode with a ramp rate of 2 K/min.

Muon spin relaxation measurements: Muon depolarization data were taken on the General Purpose Surface-muon spectrometer on the πM3.2 beamline at the Paul Scherrer Institute. For the zero-field data the muon beam spin polarization was oriented at 45° to the muon momentum, while for longitudinal field studies the polarization was anti-parallel to the momentum. A pressed powder disk of diameter 10 mm and thickness 2 mm was wrapped in thin mylar foil and suspended in a gas-flow cryostat. Data were fit using the MUSRFIT program[49] and supporting fit parameters are presented in Supplemental Figure 3.

Electronic structure calculations: First-principles electronic calculations based on density functional theory (DFT) were performed using the Vienna ab initio Simulation Package (VASP version 5.4.4) [50,51] with the local density approximation functional and projector-augmented wave (PAW) pseudopotentials.[52,53] The plane-wave energy cutoff was set to 400 eV and a Γ-centered 15 × 15 × 15 k-point mesh was automatically generated within VASP. Initial biasing of the spin-polarization and tetrahedral smearing with Blöchl corrections were used for the self-consistent static calculation.[54] The electronic structure was calculated via a non-self-consistent run using the charge density from the static calculation with spin-orbit coupling (SOC) and a Hubbard U correction of 1 eV. A k-point path for the band structure calculation was generated using the AFLOW online tool.[55] All calculations had energy convergence better than 10^{-6} eV.

Data Availability: The data that support the findings of this study are available at https://doi.org/10.25349/D9R626 .

Acknowledgments: We thank Roser Valentí and Liviu Hozoi for sharing preliminary *ab initio* calculations of magnetic exchange interactions. This work was supported by DOE, Office of Science, Basic Energy Sciences under Award DE-SC0017752 (S.D.W., B.R.O., P.M.S.). Work by L.B. was supported by the DOE, Office of Science, Basic Energy Sciences under Award No. DE-FG02-08ER46524. Part of this work is based on experiments performed at the Swiss Muon Source SμS, Paul Scherrer Institute, Villigen, Switzerland. R.S. and A.H. acknowledge support from the National Science Foundation (NSF) through Enabling Quantum Leap: Convergent Accelerated Discovery Foundries for Quantum Materials Science, Engineering and Information (Q-AMASE-i): Quantum Foundry at UC Santa Barbara (DMR-1906325). A portion of this research used resources at the High Flux Isotope Reactor and Spallation Neutron Source, a DOE Office of Science User Facility operated by the Oak Ridge National Laboratory. Use of the Advanced Photon Source at Argonne National Laboratory was supported by the U. S. Department of Energy, Office of Science, Office of Basic Energy Sciences, under Contract No. DE-AC02-06CH11357. We thank NIST for access to their neutron facilities Certain commercial equipment, instruments, or materials are identified in this document. Such identification does not imply recommendation or endorsement by the National Institute of Standards and Technology, nor does it imply that the products identified are necessarily the best available for the purpose.

Author Contributions: S.D.W. wrote the manuscript with input from all coauthors. B.R.O., P.M.S., and A.H. synthesized the material and performed resistivity, magnetization, and neutron scattering measurements. A.H. and R.S. performed *ab initio* DFT calculations. E.K., M.J.G., and C.W. performed muon spin relaxation measurements. A.K., C.M.B., D.M.P., K.M.T., and A.A. performed neutron scattering measurements. L.B. provided theoretical insight into modeling the material. All authors participated in planning and discussions of experiments.

Additional Information: Supplementary Information accompanies this paper.

Competing interests: The authors declare no competing financial or non-financial interests.

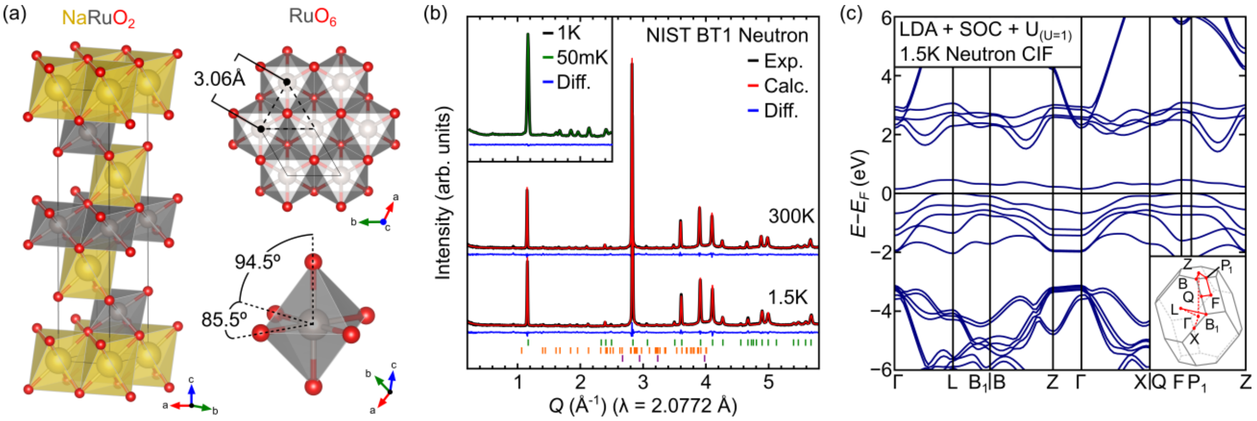

Figure 1: Lattice and electronic band structures of NaRuO$_2$ (a) Crystal lattice of NaRuO$_2$ that forms in the $R\bar{3}m$ space group showing the triangular lattice of edge-sharing RuO$_6$ octahedra arranged in a layered structure separated by planes of Na-ions. The slight trigonal distortion of the RuO$_6$ octahedra is illustrated. (b) Neutron powder diffraction data collected at 300 K, 1.5 K, 1 K, and 50 mK. Data in the main panel were collected at BT-1 and are overplotted with the refined structural diffraction pattern. The pattern includes NaRuO$_2$ (96.7% by weight) indexed by the top row of green ticks, Na$_2$CO$_3$ (2.9%) indexed with the middle row of orange ticks, and Ru metal (0.4%) indexed with the bottom row of purple ticks. We note that powder samples prepared with higher purity Na$_2$O$_2$ starting reagents do not show this small fraction of Na$_2$CO$_3$ impurity and exhibit the same properties as those reported here. The inset shows data collected on HB-1A and reveals no magnetic scattering appearing down to 50 mK. The direct subtraction of the 1 K and 50 mK data is shown by the featureless blue line. (c) LDA electronic band structure for NaRuO$_2$ using both λ and U=1 eV. The inset shows the high symmetry positions in the Brillouin zone.

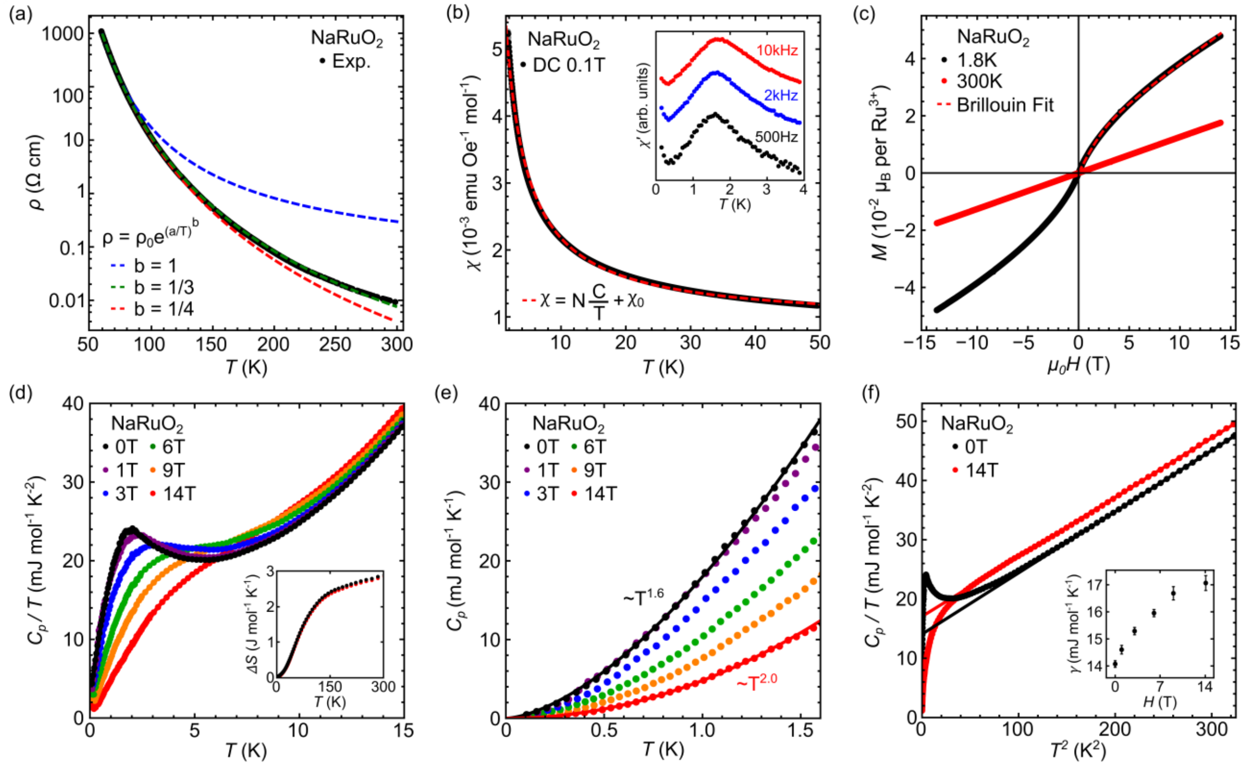

Figure 2: Electrical transport, magnetic susceptibility, and heat capacity data characterizing the low temperature properties of NaRuO$_2$ (a) DC resistivity data collected as a function of temperature. Fits to models of variable-range hopping transport are overpotted for both two-dimensional (b=1/3) and three-dimensional forms (b=1/4) as well as a fit to a conventional Arrhenius (b=1) behavior (b) Low-field magnetic susceptibility (M/H) collected under $\mu_0 H$ = 0.1 T. Dashed line is a fit to a low-temperature Curie-law with the additional of a substantial Pauli-like χ_0 term. Inset shows the magnetic susceptibility measured across the partial freezing transition near 1.5K. For molar magnetic susceptibility, 1 emu/(mol Oe) = 4π 10^{-6} m^3/mol (c) Isothermal magnetization data collected at 1.8 K and 300 K. Dashed line shows a fit using a dominant, linear χ_0 term and a S=1/2 Brillouin function. (d) Isobaric heat capacity $C_p(T)$ collected under a variety of magnetic fields. Inset shows the magnetic entropy extracted via removal of the nonmagnetic analog NaRhO$_2$. (e) Low-temperature heat capacity collected below the crossover at 1.5 K. Power-law fits are shown as solid lines (f) $C_p(T)/T$ plotted as a function of T^2. Solid lines are fits to the model described in the text. Inset shows the evolution of the effective Sommerfeld coefficients under the application of a magnetic field. Error bars represent one standard deviation.

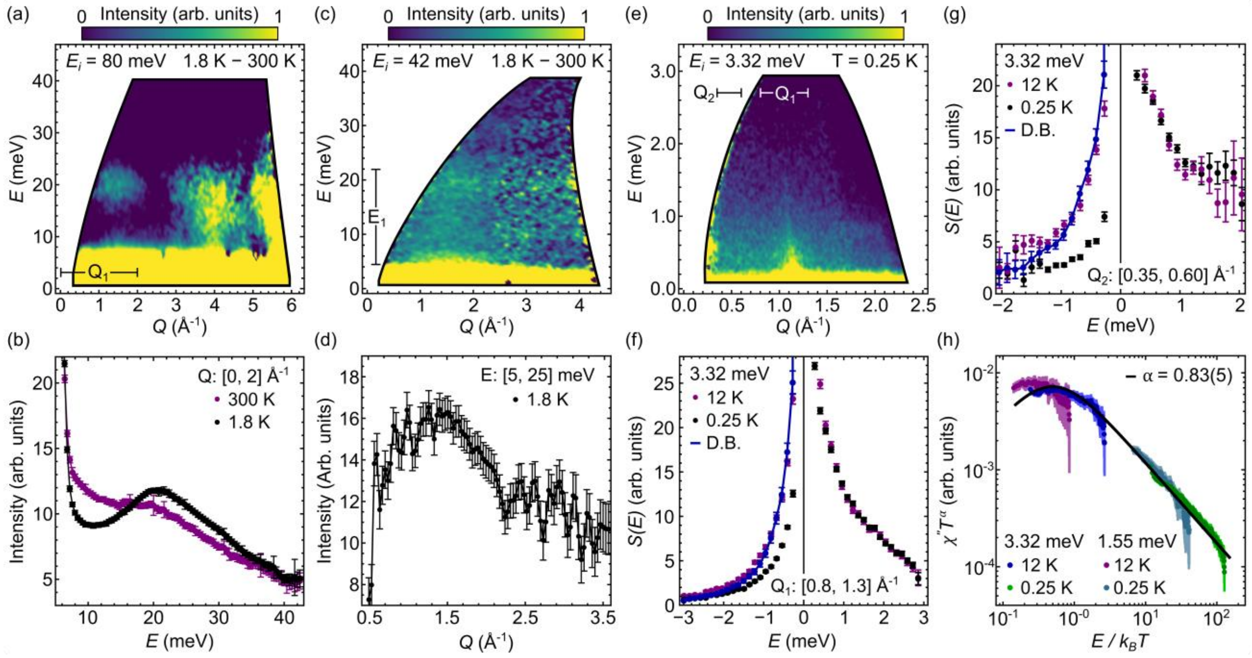

Figure 3: Inelastic neutron scattering data collected on NaRuO$_2$ (a) Energy-momentum map of scattering intensity collected with E_i=80 meV at 1.8 K with the 300 K data subtracted after correcting for the Bose population factor. (b) Momentum-averaged energy cut through the temperature subtracted map plotted in panel (a), (c) Energy-momentum map of scattering intensity collected with E_i=42 meV at 1.8 K with the 300 K data subtracted after removing the Bose population factor (d) Energy-averaged momentum cut through the map plotted in panel (c). (e) Low energy (E_i=3.32 meV) energy-momentum map of scattering intensity collected at 1.8 K. Momentum-averaged energy cuts at 250 mK and 12 K collected about 1.1 Å^{-1} and 0.475 Å^{-1} are plotted in panels (f) and (g) respectively. Solid lines represent the expectation of scattering intensities at 12 K for E<0 based on the detailed balance relation for excitations measured at 12 K with E>0, where $S(Q,-E) = S(Q,E)e^{\frac{-E}{k_B T}}$. (h) Quantum critical scaling plot using momentum-averaged energy cuts about 1.1 Å^{-1} collected with E_i=3.32 meV and E_i=1.55 meV at various temperatures. Data were converted to $\chi''(Q,\omega)$ and scaled as described in the text. The solid line represents the test scaling function described in the text. Error bars in all panels represent one standard deviation.

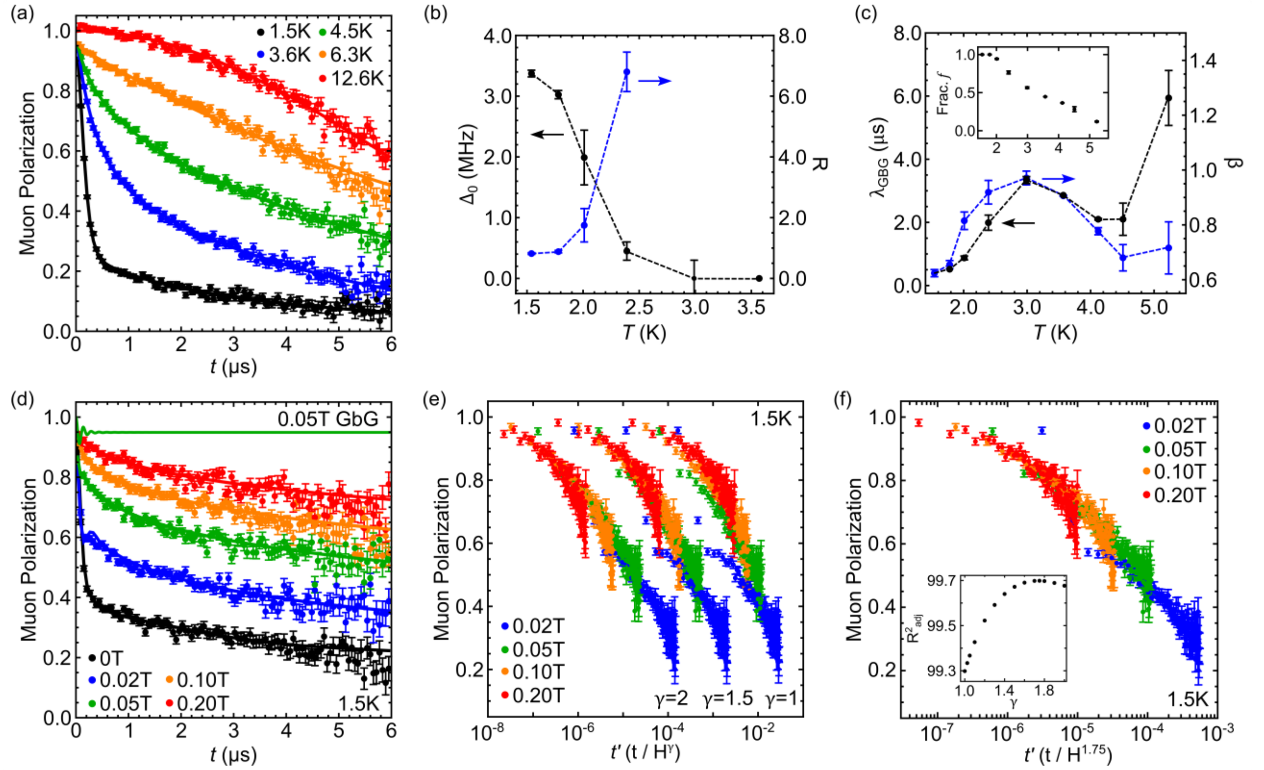

Figure 4: Muon spin relaxation data and analysis (a) Zero-field muon spin relaxation collected for a variety of temperatures. (b), (c) Fit values for the zero-field muon spin relaxation model described in the text. (d) Muon spin relaxation data collected at 1.5 K under a variety of applied longitudinal fields; the solid green curve is the calculated response for a fully static GbG function for the zero-field fit parameters and γ_{GbG} set to 0 at T=1.5 K. (e) 1.5 K muon polarization under varying longitudinal field strengths plotted with different exponents of t/H^{γ}. (f) Scaling collapse of 1.5 K longitudinal field data for an exponent of γ=1.75. Inset: Goodness of fit of the data to a 3rd order polynomial as a function of γ. Error bars represent one standard deviation.

References:

[1] Hidekazu Morita, Shinji Watanabe and Masatoshi Imada, “Nonmagnetic Insulating States near the Mott Transitions on Lattices with Geometrical Frustration and Implications for κ-$(ET)_2Cu_2(CN)_3$” Journal of the Physical Society of Japan 71, 2109 (2002).

[2] Peyman Sahebsara and David Senechal “Hubbard Model on the Triangular Lattice: Spiral Order and Spin Liquid” Physical Review Letters 100, 136402 (2008).

[3] Manuel Laubach, Ronny Thomale, Christian Platt, Werner Hanke, and Gang Li “Phase diagram of the Hubbard model on the anisotropic triangular lattice” Physical Review B 91, 245125 (2015).

[4] Satoshi Yamashita, Yasuhiro Nakazawa, Masaharu Oguni, Yugo Oshima, Hiroyuki Nojiri, Yasuhiro Shiizu, Kazuya Miyagawa, and Kazushi Kanoda “ Thermodynamic properties of a spin-1/2 spin-liquid state in a κ-type organic salt” Nature Physics 4, 459 (2008).

[5] Takayuki Isono, Hiromichi Kamo, Akira Ueda, Kazuyuki Takahashi, Motoi Kimata, Hiroyuki Tajima, Satoshi Tsuchiya, Taichi Terashima, Shinya Uji, and Hatsumi Mori, “Gapless Quantum Spin Liquid in an Organic Spin-1/2 Triangular-Lattice κ − H_3(Cat-EDT-TTF)$_2$” Physical Review Letters 112, 177201 (2014).

[6] Itou, T.; Oyamada, A.; Maegawa, S.; Tamura, M.; Kato, R. “Quantum spin liquid in the spin-1/2 triangular antiferromagnet EtMe3Sb[Pd(dmit)2]2” Phys. Rev. B 77, 104413 (2008).

[7] Y. Shimizu, K. Miyagawa, K. Kanoda, M. Maesato, and G. Saito, “Spin Liquid State in an Organic Mott Insulator with a Triangular Lattice” Physical Review Letters 91, 107001 (2003).

[8] Mitchell M. Bordelon, Eric Kenney, Chunxiao Liu, Tom Hogan, Lorenzo Posthuma, Marzieh Kavand, Yuanqi Lyu et al. "Field-tunable quantum disordered ground state in the triangular-lattice antiferromagnet $NaYbO_2$." Nature Physics 15, 1058 (2019).

[9] Andrew Peter Mackenzie "The properties of ultrapure delafossite metals." Reports on Progress in Physics 80, 032501 (2017).

[10] M. F. Collins, and O. A. Petrenko. "Review/synthèse: Triangular antiferromagnets." Canadian Journal of Physics 75, 605 (1997).

[11] Kim, B. J., Hosub Jin, S. J. Moon, J-Y. Kim, B-G. Park, C. S. Leem, Jaejun Yu et al. "Novel J_{eff}= 1/2 Mott state induced by relativistic spin-orbit coupling in Sr_2IrO_4." Physical review letters 101, 076402 (2008).

[12] S. J. Moon, Hosub Jin, Kyung Wan Kim, W. S. Choi, Y. S. Lee, Jaejun Yu, G. Cao et al. "Dimensionality-Controlled Insulator-Metal Transition and Correlated Metallic State in 5 d Transition Metal Oxides $Sr_{n+1}Ir_nO_{3n+1}$ (n= 1, 2, and ∞)." Physical Review Letters 101, 226402 (2008).

[13] K. W. Plumb, J. P. Clancy, L. J. Sandilands, V. Vijay Shankar, Y. F. Hu, K. S. Burch, Hae-Young Kee, and Young-June Kim “α−$RuCl_3$: A spin-orbit assisted Mott insulator on a honeycomb lattice” Phys. Rev. B 90, 041112(R) (2014).

[14] Ravi Yadav, Nikolay A. Bogdanov, Vamshi M. Katukuri, Satoshi Nishimoto, Jeroen van den Brink and Liviu Hozoi “Kitaev exchange and field-induced quantum spin-liquid states in honeycomb α-$RuCl_3$” Scientific Reports 6, 37925 (2016).

[15] A. Koitzsch, C. Habenicht, E. Müller, M. Knupfer, B. Büchner, H. C. Kandpal, J. van den Brink, D. Nowak, A. Isaeva, and Th. Doert “J_{Eff} Description of the Honeycomb Mott Insulator α−RuCl3” Phys. Rev. Lett. 117, 126403 (2016).

[16] Masahiro Shikano, Claude Delmas, and Jacques Darriet “$NaRuO_2$ and $Na_xRuO_2\,{}_yH_2O$: New Oxide and Oxyhydrate with Two Dimensional RuO_2 Layers” Inorganic Chemistry 43, 1214 (2004).

[17] Yang, Hong-Yu, Andreas M. Läuchli, Frédéric Mila, and Kai Phillip Schmidt. "Effective spin model for the spin-liquid phase of the Hubbard model on the triangular lattice." Physical Review Letters 105, 267204 (2010).

[18] Pavel Kos, and Matthias Punk. "Quantum spin liquid ground states of the Heisenberg-Kitaev model on the triangular lattice." Physical Review B 95, 024421 (2017).

[19] Kai Li, Shun-Li Yu, and Jian-Xin Li. "Global phase diagram, possible chiral spin liquid, and topological superconductivity in the triangular Kitaev–Heisenberg model." New Journal of Physics 17, 043032 (2015).

[20] Brenden R. Ortiz, Paul M. Sarte, Alon H. Avidor, and Stephen D. Wilson, “Defect control in the Heisenberg-Kitaev candidate material $NaRuO_2$” Phys. Rev. Materials 6, 104413 (2022).

[21] Soobin Sinn, Choong Hyun Kim, Beom Hyun Kim, Kyung Dong Lee, Choong Jae Won, Ji Seop Oh, Moonsup Han, Young Jun Chang, Namjung Hur, Hitoshi Sato, Byeong-Gyu Park, Changyoung Kim, Hyeong-Do Kim, and Tae Won

Noh “Electronic Structure of the Kitaev Material α-RuCl3 Probed by Photoemission and Inverse Photoemission Spectroscopies” Scientific Reports 6, 39544 (2016).

[22] H. C. Jamieson and F D Manchester “The magnetic susceptibility of Pd, PdH and PdD between 4 and 300 K” J. Phys. F: Met. Phys. 2, 323 (1972).

[23] Stacey J. Smith, Rebecca Stevens, Shengfeng Liu, Guangshe Li, Alexandra Navrotsky, Juliana Boerio-Goates, and Brian F. Woodfield. "Heat capacities and thermodynamic functions of TiO_2 anatase and rutile: Analysis of phase stability." American Mineralogist 94, 236 (2009).

[24] Jacob M. Schliesser and Brian F. Woodfield “Lattice vacancies responsible for the linear dependence of the low-temperature heat capacity of insulating materials” Physical Review B 91, 024109 (2015).

[25] Satoshi Yamashita, Yasuhiro Nakazawa, Masaharu Oguni, Yugo Oshima, Hiroyuki Nojiri, Yasuhiro Shimizu, Kazuya Miyagawa, and Kazushi Kanoda “Thermodynamic properties of a spin-1/2 spin-liquid state in a κ-type organic salt” Nature Physics 4, 459 (2008).

[26] J. M. Ni, B. L. Pan, B. Q. Song, Y. Y. Huang, J. Y. Zeng, Y. J. Yu, E. J. Cheng, L. S. Wang, D. Z. Dai, R. Kato, and S. Y. Li “Absence of Magnetic Thermal Conductivity in the Quantum Spin Liquid Candidate EtMe3Sb[Pd(dmit)2]2” Phys. Rev. Lett. 123, 247204 (2019)

[27] Satoshi Yamashita, Takashi Yamamoto, Yasuhiro Nakazawa, Masafumi Tamura, and Reizo Kato “Gapless spin liquid of an organic triangular compound evidenced by thermodynamic measurements” Nature Communications 2, 275 (2011).

[28] A. Schröder, G. Aeppli, E. Bucher, R. Ramazashvili, and P. Coleman “Scaling of Magnetic Fluctuations near a Quantum Phase Transition” Phys. Rev. Lett. 80, 5623 (1998).

[29] Subir Sachdev and Jinwu Ye. "Universal quantum-critical dynamics of two-dimensional antiferromagnets." Physical review letters 69, 2411 (1992).

[30] D. R. Noakes and G. M. Kalvius “Anomalous zero-field muon spin relaxation in highly disordered magnets” Physical Review B 56, 2352 (1997).

[31] J. A. Hodges, P. Bonville, A. Forget, A. Yaouanc, P. Dalmas de Réotier, G. André, M. Rams, K. Królas, C. Ritter, P. C. M. Gubbens, C. T. Kaiser, P. J. C. King, and C. Baines “First-Order Transition in the Spin Dynamics of Geometrically Frustrated $Yb_2Ti_2O_7$” Physical Review Letters 88, 077204 (2002).

[32] Y. J. Uemura, A. Keren, K. Kojima, L. P. Le, G.M. Luke, W. D. Wu, Y. Ajiro, T. Asano, Y. Kuriyama, M. Mekata, H. Kikuchi, and K. Kakurai, Phys. Rev. Lett. 73, 3306 (1994).

[33] Rebecca Dally, Tom Hogan, Alex Amato, Hubertus Luetkens, Chris Baines, Jose Rodriguez-Rivera, Michael J. Graf, and Stephen D. Wilson, “Short-range correlations in the magnetic ground state of $Na_4Ir_3O_8$”, Physical Review Letters 113, 247601 (2014).

[34] Shockley, A. C., F. Bert, J. C. Orain, Y. Okamoto, and P. Mendels. "Frozen state and spin liquid physics in $Na_4Ir_3O_8$: An NMR study." Physical Review Letters 115, 047201 (2015).

[35] Amit Keren. "Muons as probes of dynamical spin fluctuations: some new aspects." Journal of Physics: Condensed Matter 16, S4603 (2004).

[36] Amit Keren, Philippe Mendels, Ian A. Campbell, and James Lord “Probing the Spin-Spin Dynamical Autocorrelation Function in a Spin Glass above T_g via Muon Spin Relaxation” Physical Review B 77, 1386 (1996).

[37] Keith Robinson, G. V. Gibbs, and P. H. Ribbe. "Quadratic elongation: a quantitative measure of distortion in coordination polyhedra." Science 172, no. 3983 (1971): 567-570.

[38] Feng Ye, Songxue Chi, Huibo Cao, Bryan C. Chakoumakos, Jaime A. Fernandez-Baca, Radu Custelcean, T. F. Qi, O. B. Korneta, and G. Cao “Direct evidence of a zigzag spin-chain structure in the honeycomb lattice: A neutron and x-ray diffraction investigation of single-crystal Na_2IrO_3” Phys. Rev. B 85, 180403(R) (2012).

[39] Sae Hwan Chun, Jong-Woo Kim, Jungho Kim, H. Zheng, Constantinos C. Stoumpos, C. D. Malliakas, J. F. Mitchell et al. "Direct evidence for dominant bond-directional interactions in a honeycomb lattice iridate Na2IrO3." Nature Physics 11, 462 (2015).

[40] Arnab Banerjee, Jiaqiang Yan, Johannes Knolle, Craig A. Bridges, Matthew B. Stone, Mark D. Lumsden, David G. Mandrus, David A. Tennant, Roderich Moessner, and Stephen E. Nagler. "Neutron scattering in the proximate quantum spin liquid α-RuCl3." Science 356, 1055 (2017).

[41] Huibo Cao, B., A. Banerjee, J-Q. Yan, C. A. Bridges, M. D. Lumsden, D. G. Mandrus, D. A. Tennant, B. C. Chakoumakos, and S. E. Nagler. "Low-temperature crystal and magnetic structure of α− RuCl 3." Physical Review B 93, 134423 (2016).

[42] Ye, Feng, Songxue Chi, Huibo Cao, Bryan C. Chakoumakos, Jaime A. Fernandez-Baca, Radu Custelcean, T. F. Qi, O. B. Korneta, and Gang Cao. "Direct evidence of a zigzag spin-chain structure in the honeycomb lattice: A neutron and x-ray diffraction investigation of single-crystal Na2IrO3." Physical Review B 85, 180403 (2012).

[43] Sung-Sik Lee, and Patrick A. Lee. "U (1) gauge theory of the Hubbard model: Spin liquid states and possible application to κ−(BEDT− TTF) 2 Cu 2 (CN) 3." Physical review letters 95, 036403 (2005).

[44] I. Motrunich, Olexei "Variational study of triangular lattice spin-1∕ 2 model with ring exchanges and spin liquid state in κ−(ET) 2 Cu 2 (CN) 3." Physical Review B 72, 045105 (2005).

[45] Louisiane Verger, Marie Guignard, and Claude Delmas, "Sodium Electrochemical Deintercalation and Intercalation in O3-NaRhO$_2$ and P2-NaxRhO$_2$ Layered Oxides" Inorg. Chem. 58, 2543 (2019).

[46] G. E. Granroth, A. I. Kolesnikov, T. E. Sherline, J. P. Clancy, K. A. Ross, J. P. C. Ruff, B. D. Gaulin, and S. E. Nagler, "SEQUOIA: a newly operating chopper spectrometer at the SNS," J. Physics: Conference Series 251, 012058 (2010).

[47] G. Ehlers, A. A. Podlesnyak, and A. I. Kolesniko "The cold neutron chopper spectrometer at the Spallation Neutron Source—A review of the first 8 years of operation" Review of Scientific Instruments 87, 093902 (2016).

[48] Gordon A. Bain and John F. Berry, "Diamagnetic Corrections and Pascal's Constants" Journal of Chemical Education 85, 532 (2008).

[49] A. Suter and B. M. Wojek, Phys. Procedia 30, 69 (2012).

[50] G. Kresse and J. Furthmüller "Efficient iterative schemes for ab initio total-energy calculations using a plane-wave basis set" Phys. Rev. B 54, 11169 (1996).

[51] G. Kressea and J. Furthmüller "Efficiency of ab-initio total energy calculations for metals and semiconductors using a plane-wave basis set" Computational Materials Science 6, 15 (1996).

[52] P. E. Blöchl "Projector augmented-wave method" Phys. Rev. B 50, 17953 (1994)

[53] G. Kresse and D. Joubert "From ultrasoft pseudopotentials to the projector augmented-wave method" Phys. Rev. B 59, 1758 (1999).

[54] Peter E. Blöchl, O. Jepsen, and O. K. Andersen "Improved tetrahedron method for Brillouin-zone integrations" Phys. Rev. B 49, 16223 (1994).

[55] Wahyu Setyawan and Stefano Curtarolo "High-throughput electronic band structure calculations: Challenges and tools" Computational Materials Science 49, 299 (2010).

Supplemental Information

Quantum Disordered Ground State in the Triangular Lattice Magnet $NaRuO_2$

Brenden R. Ortiz[1#], Paul Sarte[1#], Alon Hendler Avidor[1], Aurland Hay[1], Eric Kenney[2], Alexander I. Kolisneikov[3], Daniel M. Pajerowski[3], Adam A. Aczel[3], Keith M. Taddei[3], Craig M. Brown[4,5], Chennan Wang[6], Michael J. Graf[2], Ram Seshadri[1], Leon Balents[7], Stephen D. Wilson[1*]

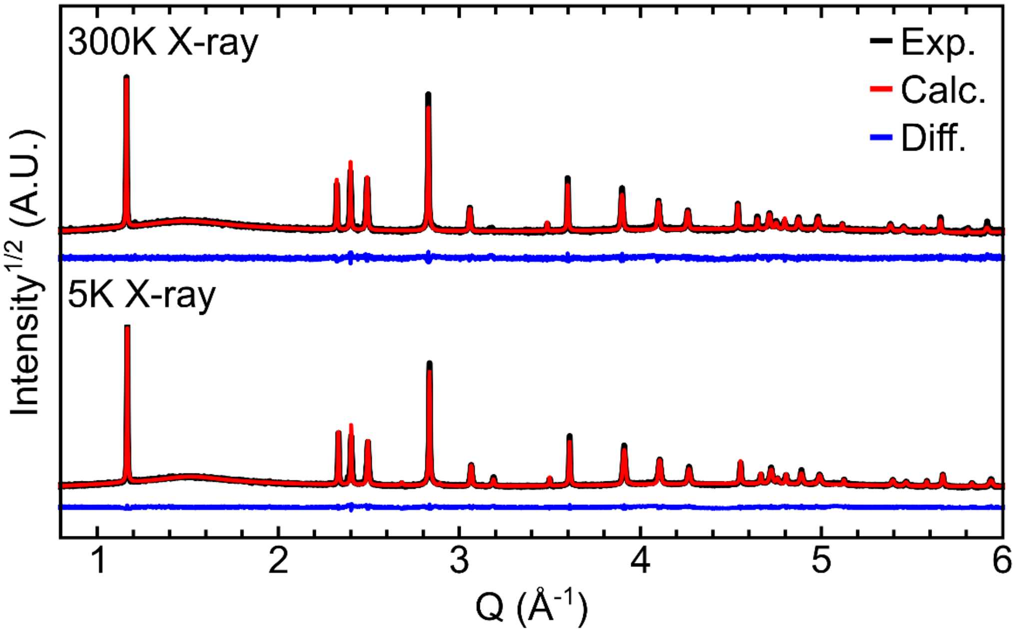

Supplemental Figure 1: X-ray diffraction data collected at 5 K and 300 K. Red lines show the output of the structural refinement model and blue lines denote the difference between the model and the data. Synchrotron x-ray data were collected at 11-BM at the Advanced Photon Source.

NaRuO$_2$ (BT1 300K)

a (Å)	c (Å)	V (Å^3)	c/a	α (°)
3.061039(82)	16.179435(467)	131.290(8)	5.29	94.7

site	x	y	z	Occ	B$_{eq}$
Ru	0	0	0.5	1.0	2.20(4)
Na	0	0	0	1.0	3.79(8)
O	0	0	0.23470(6)	1.0	1.75(3)

NaRuO$_2$ (BT1 1.5K)

a (Å)	c (Å)	V (Å^3)	c/a	α (°)
3.055783(95)	16.122636(506)	130.380(9)	5.28	94.8

site	x	y	z	Occ	B$_{eq}$
Ru	0	0	0.5	1.0	2.00(4)
Na	0	0	0	1.0	2.97(8)
O	0	0	0.23448(7)	1.0	1.52(4)

NaRuO$_2$ (APS 300K)

a (Å)	c (Å)	V (Å^3)	c/a	α (°)
3.065374(21)	16.228787(179)	132.064(2)	5.29	93.7

site	x	y	z	Occ	B$_{eq}$
Ru	0	0	0.5	1.0	2.31(5)
Na	0	0	0	1.0	3.68(9)
O	0	0	0.23641(42)	1.0	1.79(9)

NaRuO$_2$ (APS 5K)

a (Å)	c (Å)	V (Å^3)	c/a	α (°)
3.060344(13)	16.162925(101)	131.096(1)	5.28	95.2

site	x	y	z	Occ	B$_{eq}$
Ru	0	0	0.5	1.0	2.01(2)
Na	0	0	0	1.0	3.16(5)
O	0	0	0.23365(17)	1.0	1.84(9)

Supplemental Table 1: Crystallographic parameters for NaRuO$_2$ using both neutron and synchrotron diffraction data. Occupancy values refine to within unity and were fixed for later analysis. For synchrotron data, the B$_{eq}$ for oxygen was constrained near that of the neutron data. Values in parenthesis are one standard deviation. Refinement GOF is between 1.8-1.9 for all refinements.

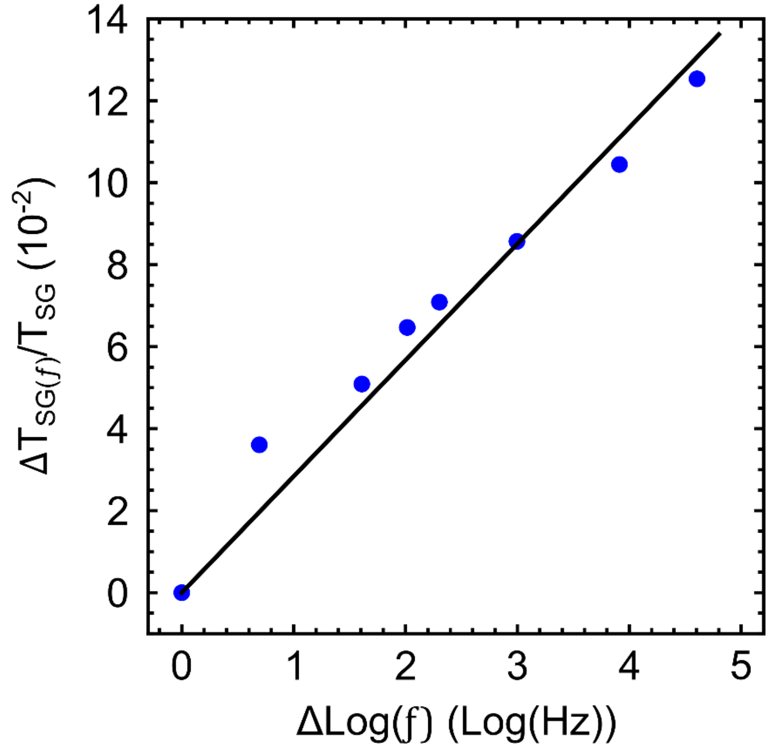

Supplemental Figure 2: Frequency dependence of the low-temperature cusp in the AC susceptibility of $NaRuO_2$. The resulting Mydosh parameter $K = \frac{\Delta T_f}{T_f \log(\Delta f)} = 0.028$ is an unusual intermediate value. It is significantly smaller than that expected for a superparamagnet and significantly larger than that expected for a conventional spin glass.[1,2,3] This weak freezing represents a small amount of entropy and marks a crossover into a state with persistent spin fluctuations as described in the main text of the manuscript.

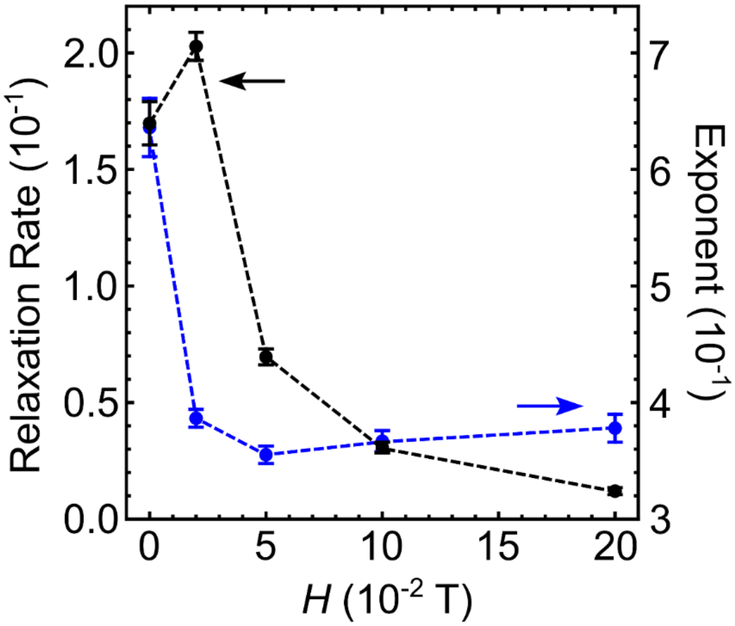

Supplemental Figure 3: Fit parameters resulting from the model of the longitudinal field muon spin polarization data at 1.5 K where the polarization is parameterized by the form $P(t) = GbG(\Delta; R; t)e^{(-\lambda_{GbG}t)^{\beta}}$. The relaxation rate λ_{GBG} (left axis) and stretched exponent β (right axis) are plotted as a function of the applied longitudinal magnetic field. Error bars represent one standard deviation in the parameters derived from nonlinear least square fits to the data.

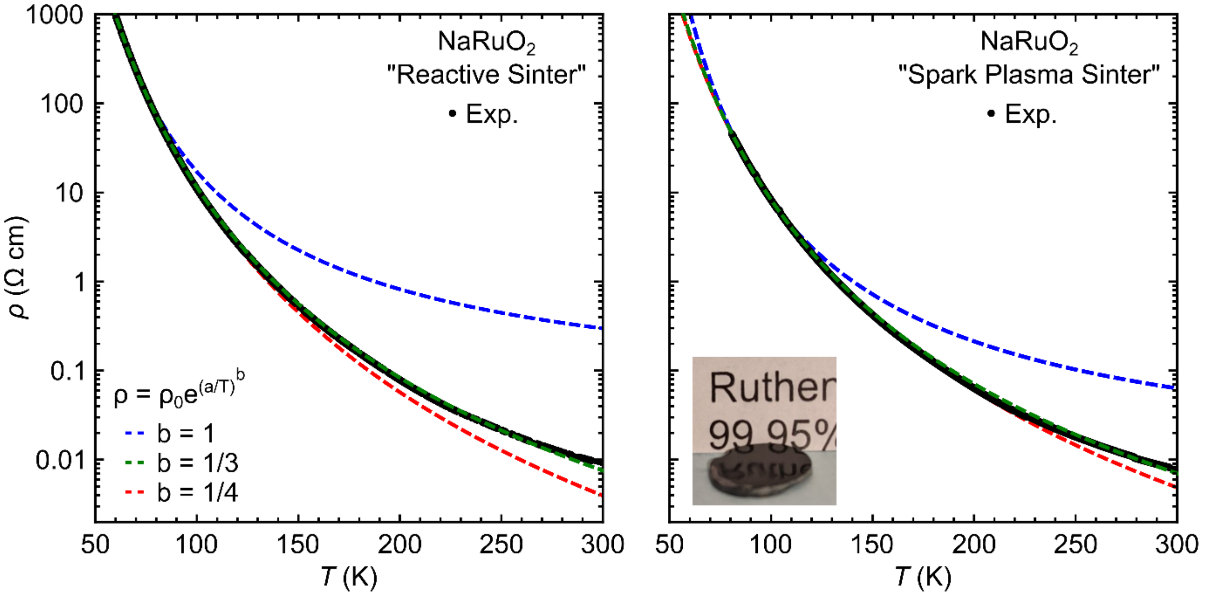

Supplemental Figure 4: Comparison of electrical transport data between the samples prepared via a cold-press plus reactive sinter as presented in the main text and via spark plasma sintering (SPS) which provides an even higher pellet density. The left panel shows temperature dependent resistivity from a reactive sinter sample while the right panel shows the results from the SPS sample. The inset shows a mirror surface finish once polished, demonstrating the high density of the sample. Dashed lines are fits to the transport models described in the main text.

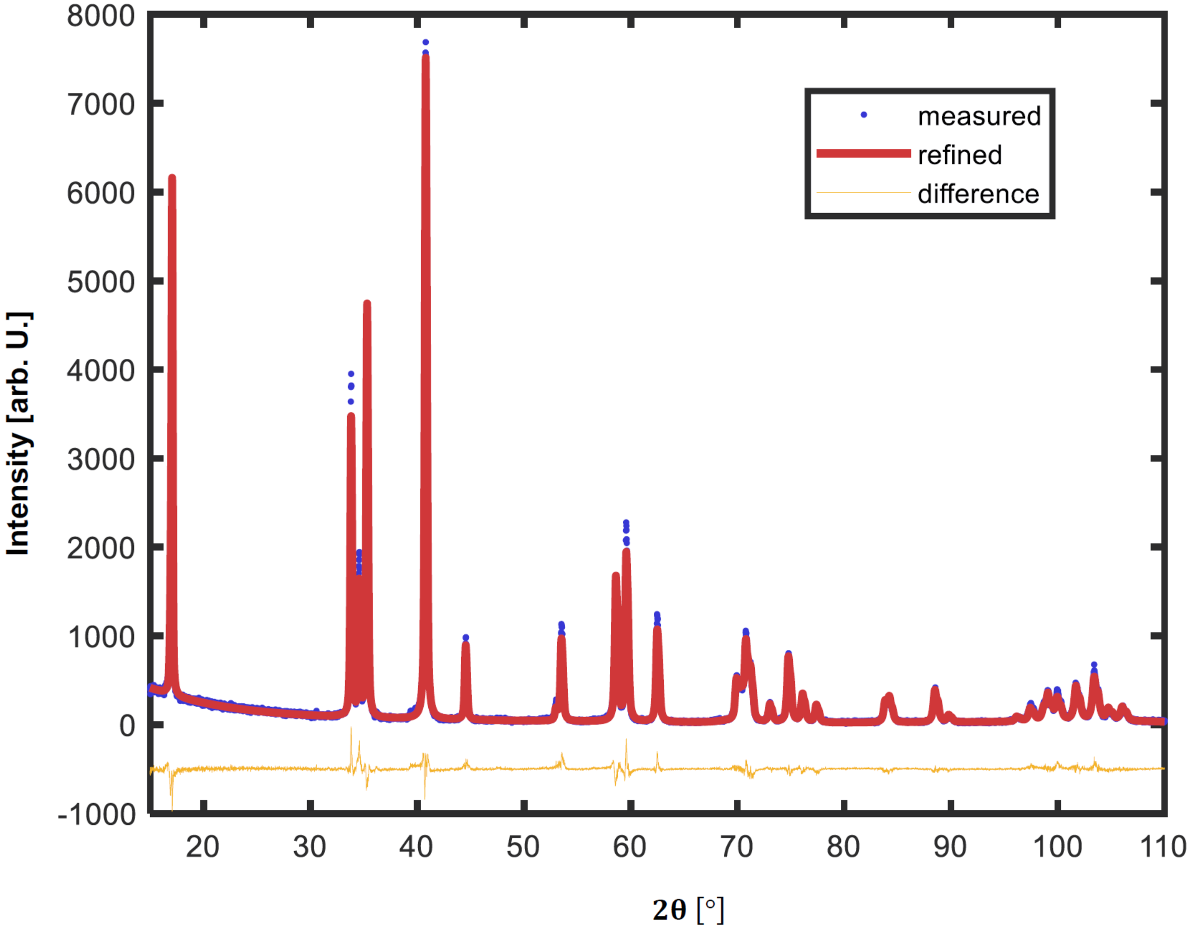

Supplemental Figure 5: $NaRhO_2$ x-ray powder diffraction data characterizing the phase purity of powder used as a phonon reference for magnetic entropy calculations. The red line shows the results of Rietveld refinement of the powder pattern and the yellow line shows the difference between the data and the Rietveld model. Data were collected using a Panalytical Empyrean diffractometer (Cu Kα, 1.54 Å) in the Bragg-Brentano geometry

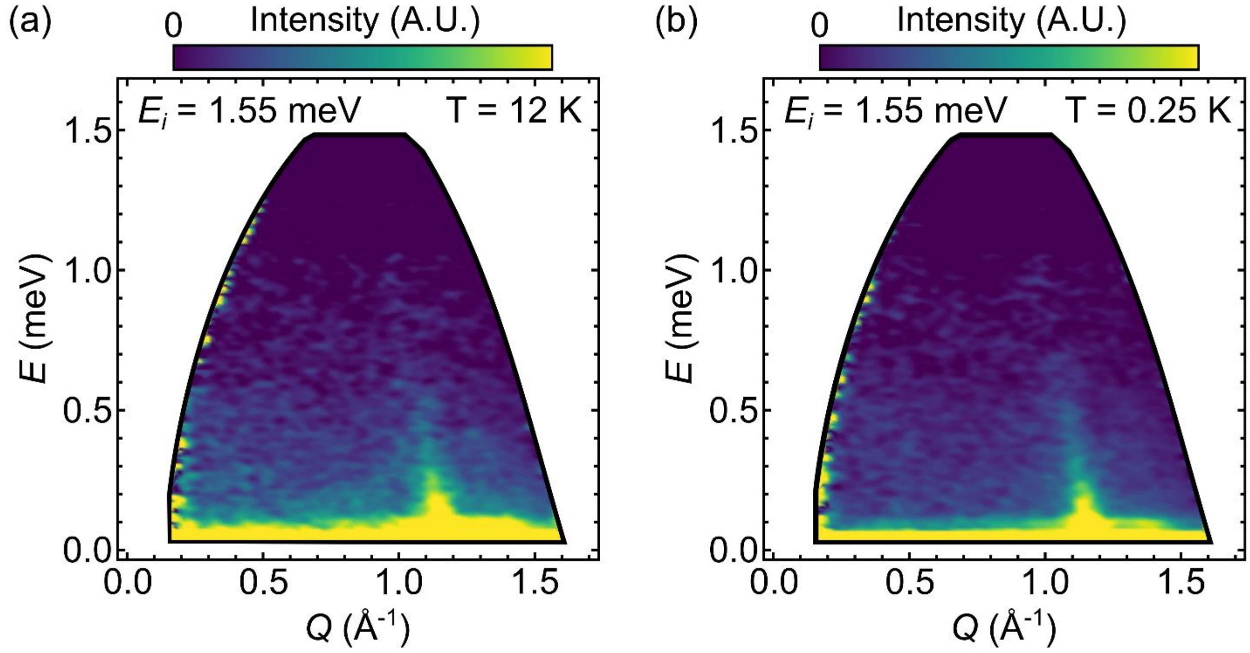

Supplemental Figure 6: Momentum and energy maps of neutron scattering $I(Q,\omega)$ collected at (a) 250 mK and (b) 12 K with an incident energy E_i=1.55 meV on $NaRuO_2$ powder as described in the main text. The narrow, slightly sloping tail centered near Q=1.2 Å^{-1} arises from the CNCS resolution ellipsoid catching portion of the nuclear Bragg peak and quasielastic scattering.

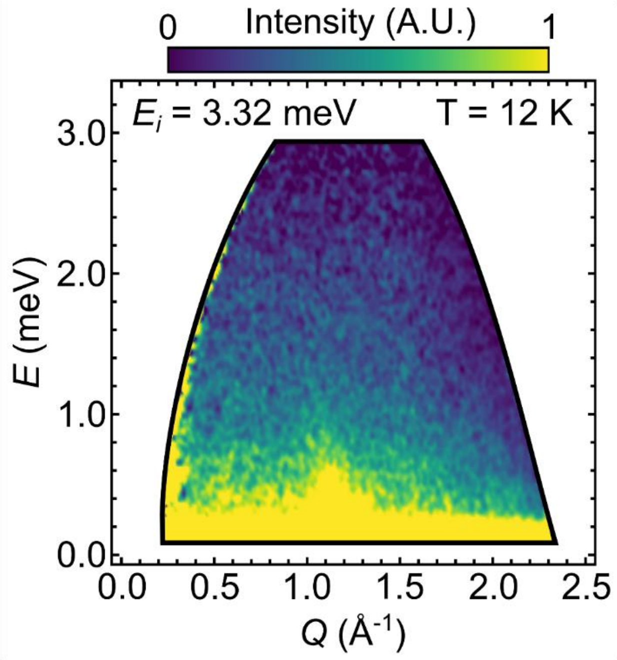

Supplemental Figure 7: Momentum and energy map of neutron scattering $I(Q,\omega)$ collected at 12 K with an incident energy E_i=3.32 meV on $NaRuO_2$ powder as described in the main text.

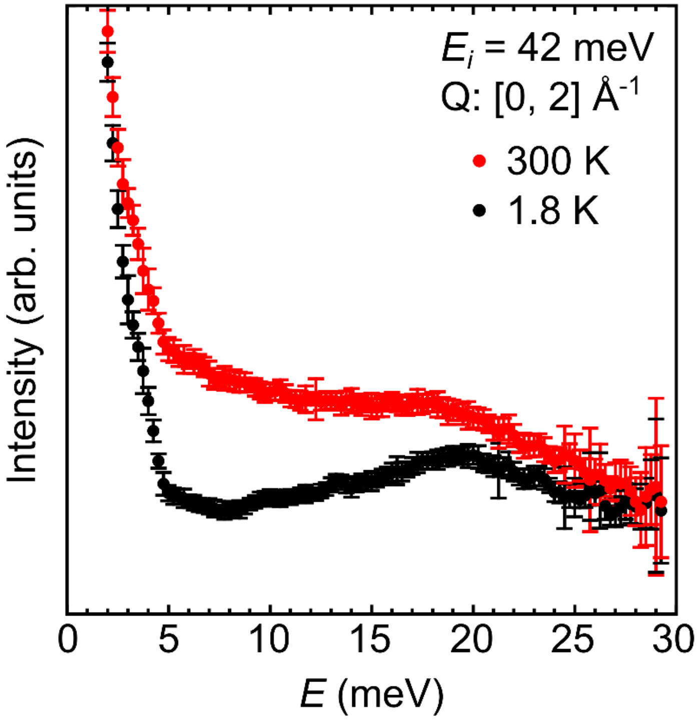

Supplemental Figure 8: Momentum-averaged cut through scattering $S(Q,\omega)$ collected at 1.8 K and 300K with an incident energy E_i=42 meV on $NaRuO_2$ powder as described in the main text. Error bars in all panels represent one standard deviation in the data based on Poissonian statistics with the sample size being the neutron counts.

References:

[1] H D Zhou, C R Wiebe, A Harter, N S Dalal, and J S Gardner "Unconventional spin glass behavior in the cubic pyrochlore $Mn_2Sb_2O_7$" J. Phys.: Condens. Matter 20, 325201 (2008).

[2] Johannes Kroder, Johannes Gooth, Walter Schnelle, Gerhard H. Fecher, and Claudia Felser "Observation of spin glass behavior in chiral $Mn_{48}Fe_{34}Si_{18}$ with a β-Mn related structure" AIP Advances 9, 055327 (2019).

[3] J. A. Mydosh Spin Glasses: An Experimental Introduction (1993).